Science and Technology of Advanced Materials

ISSN: 1468-6996 (Print) 1878-5514 (Online) Journal homepage: www.tandfonline.com/journals/tsta20

Next-generation hydrogen peroxide sensors based on ordered carbonaceous frameworks derived from iron porphyrin

Akiko Yoshida, Koki Chida, Takeharu Yoshii, Shunsuke Shimizu, Hirotaka Nakatsuji, Kazuhide Kamiya, Yasuhisa Hasegawa, Tetsuji Itoh & Hirotomo Nishihara

To cite this article: Akiko Yoshida, Koki Chida, Takeharu Yoshii, Shunsuke Shimizu, Hirotaka Nakatsuji, Kazuhide Kamiya, Yasuhisa Hasegawa, Tetsuji Itoh & Hirotomo Nishihara (27 May 2025): Next-generation hydrogen peroxide sensors based on ordered carbonaceous frameworks derived from iron porphyrin, Science and Technology of Advanced Materials, DOI: 10.1080/14686996.2025.2506979

To link to this article: https://doi.org/10.1080/14686996.2025.2506979

Next-generation hydrogen peroxide sensors based on ordered carbonaceous frameworks derived from iron porphyrin

Akiko Yoshida[a,b,c], Koki Chida[b], Takeharu Yoshii[b], Shunsuke Shimizu[b], Hirotaka Nakatsuji[b], Kazuhide Kamiya[d,e], Yasuhisa Hasegawa[c], Tetsuji Itoh[c]*, and Hirotomo Nishihara[b,f]*

[a]*Techno Medica Co., Ltd., Yokohama, Kanagawa, Japan,* [b]*Institute of Multidisciplinary Research for Advanced Materials, Tohoku University, Sendai, Miyagi, Japan,* [c]*Research Institute for Chemical Process Technology, National Institute of Advanced Industrial Science and Technology (AIST), Sendai, Miyagi, Japan.* [d]*Research Center for Solar Energy Chemistry, Graduate School of Engineering Science, Osaka University, Machikaneyama, Toyonaka, Osaka, Japan,* [e]*Innovative Catalysis Science Division, Institute for Open and Transdisciplinary Research Initiatives (ICS-OTRI), Osaka University, Suita, Osaka, Japan,* [f]*Advanced Institute for Materials Research (WPI-AIMR), Tohoku University, Sendai, Miyagi, Japan.*

*E-mail: tetsu-itou@aist.go.jp (Tetsuji Itoh), hirotomo.nishihara.b1@tohoku.ac.jp (Hirotomo Nishihara).

Next-generation hydrogen peroxide sensors based on ordered carbonaceous frameworks derived from iron porphyrin

Abstract

Carbon materials with ordered frameworks and atomically dispersed metal sites, referred to as ordered carbonaceous frameworks (OCFs), have attracted considerable attention for their promising potential in fundamental research and diverse practical applications, particularly in electrocatalysis. In this work, we synthesize Fe-incorporated OCF (Fe-OCF) with a heme-like structure through structure-preserving pyrolysis of Fe-porphyrin with four ethynyl groups. Fe-OCF is characterized by its ordered microporous framework, incorporating atomically dispersed Fe(III) sites with a high content of 6.9 wt%, analogous to metal-organic frameworks. At the same time, Fe-OCF possesses the advantages of carbon materials, including chemical stability, thermal stability, and electric conductivity. Remarkably, Fe-OCF mimics the functionality of a sensor enzyme by facilitating the redox reaction of hydrogen peroxide, which is regulated by an applied potential, thereby enabling bidirectional catalytic behavior. Fe-OCF exhibits a linear reduction current response to hydrogen peroxide, underscoring its efficient electron transfer and catalytic properties. Moreover, Fe-OCF demonstrates superior stability compared to molecular Fe-porphyrin, further emphasizing its potential application as a novel hydrogen peroxide sensor. These results emphasize the significant potential of Fe-based OCFs as advanced materials for artificial enzyme applications and next-generation hydrogen peroxide sensing technology.

Keywords: word; Ordered carbonaceous frameworks, Artificial heme enzymes, Hydrogen peroxide sensor

1. Introduction

Heme, a porphyrin complex with iron as its central metal, functions as a crucial cofactor for critical biological processes. It serves as the oxygen-binding site in hemoglobin (Hb) responsible for oxygen transport, in myoglobin that enables oxygen storage, and in cytochrome P450, an enzyme involved in oxygen activation. [1-5] Heme is also the activation sites for peroxidase enzymes and electron transfer sites in cytochromes, which are both pivotal in essential redox processes within biological

systems. [6] Additionally, the heme iron complex also serves as a binding site for toxic gaseous molecules like NO and CO. When these non-oxygen gaseous molecules bind to the heme iron complex, they influence various critical physiological and pathological processes related to oxygen binding, such as mitochondrial respiration, predominantly by inhibiting these functions. [7,8] These diverse roles of heme-iron complexes emphasize their versatility and importance in maintaining biochemical and physiological functions. One area of focus in nanoscience involves emulating biological systems through nanotechnologies and exploring methods to recreate them artificially. This approach leverages the optimized structures and functions of biological systems, offering innovative solutions for challenges in medicine, materials science, and environmental sustainability.

Conventional approaches to utilizing natural hemoproteins have primarily focused on electrode reactions, such as using hemoproteins as electrodes. [9-13] For instance, Liu et al. immobilized Hb on the gold colloid modified glassy carbon electrode for hydrogen peroxide (H_2O_2) biosensor. [10] Recent research has reported the use of carbonized Hb to facilitate smooth electron transfer, with applications in fuel cell cathode electrodes and in sensors for detecting H_2O_2. [11-13] By replacing enzymes with existing catalytic processes, these approaches can harness the high selectivity and reactivity of enzymes, enabling reactions that are challenging or impossible with conventional catalysts. One challenge in using enzymes into catalysis is their limited number of active sites. For example, hemoglobin only has four binding sites which can restrict reaction efficiency. Meanwhile, studies are conducted to artificially mimic the functions of heme and analyze these models in detail. Biomimetic nanostructures for heme have been developed with demonstrated ability to selectively adsorb and desorb gases such as O_2, CO, and NO. [14] For instance, Wang conducted a study on a hemoprotein model, a type of synthetic protein that contains heme groups, where they demonstrated that heme embedded in a hydrophobic matrix of polystyrene and 1-(2-phenylethyl)-imidazole has the ability to bind both O_2 and CO. [15] Additionally, Hamachi et al. attempted to bind ruthenium bipyridine complexes to the heme of Hb to control their adsorption and desorption through light. [16] However, these systems lack the ability to organize nanocomponents in a structured manner, which is essential for achieving the complex hierarchical organization found in biological systems. The ability to create organized nanostructure is a critical requirement for reproducing the complex

functions of natural heme proteins. Therefore, conventional research has focused on utilizing hybrid materials, such as layered clay minerals and mesoporous silica, to improve selective adsorption properties, catalytic activity, and chemical stability. [17,18] These efforts have demonstrated the efficacy of hierarchical organization of heme within nanopores. However, although the hierarchical structure can be regulated by utilizing the pores or interlayer spaces of a material, achieving precise control over the interactions between molecules remains a significant challenge. To overcome these challenges, we aim to leverage molecular design to develop artificial enzymes with a greater number of reactive centers than heme proteins and hierarchical structure of molecules. Specifically, by incorporating porphyrin-based materials into electrodes, we seek to explore their potential to mimic biological reactions while preserving some aspects of the structural framework and active sites. This approach could open up new possibilities that are different from the use of protein.

Metal-organic-frameworks (MOFs) and covalent organic frameworks (COFs) have potential applications in various fields of science and technology, such as supercapacitors, electrocatalysts, and gas adsorption/separation, owing to their high porosity and large surface area. However, their chemical stability, thermal stability, and electric conductivities are much less compared to porous carbon materials. [19-22] To overcome this issue, significant efforts have been devoted to the pyrolysis of organic-based framework, resulting in the successful synthesis of functional microporous carbons. [23-25] However, when heated to high temperature, the original crystalline structures are broken down, most often leading to the formation of disordered carbon materials. On the other hand, carbon materials with ordered frameworks and atomically dispersed metal sites, referred to as ordered carbonaceous frameworks (OCFs), are highly desirable for both fundamental research and practical applications, such as electrocatalysis. [26-33] OCFs are carbon materials with three-dimensional ordered structures, high electrical conductivity and high chemical and thermal stability. As a result, they are often referred to as “MOF-like carbon materials.” Indeed, a variety of OCFs incorporating single-atomic metal species, including Ni, Fe, Co, and Cu, have been synthesized to date. [26-28,30,31]

In this study, we synthesize OCF incorporating a heme-like structure through structure-preserving pyrolysis [26,27,29] of Fe-based porphyrin with four ethynyl groups, which act as thermally polymerizable moieties. The resulting Fe-OCF offers a

promising option as an artificial enzyme due to its increased active sites compared to native heme and its inherent electrical conductivity derived from the carbonized framework. In this paper, we evaluate the potential of the Fe-OCFs synthesized in this study for use in artificial Fe protein electrodes by characterizing their material properties, fundamental electrochemical behavior, stability, and H_2O_2 sensing performance, aiming to demonstrate their suitability as H_2O_2 sensors.

2. Materials and Method

2.1. Synthesis

Synthesis of 5,10,15,20-tetrakis(4-ethynylphenyl)porphyrin (p-H-P_4e_TMS)

5,10,15,20-tetrakis(4-ethynylphenyl)porphyrin was synthesized according to the reported procedure, and the overall synthetic procedure was shown in Scheme S1 (STEP 1).[30,34]

^{1}H NMR (400 MHz, $CDCl_3$): δ 8.81 (s, 8H), 8.14 (d, 8H), 7.86 (d, 8H), 3.33 (s, 4H), 0.25 (s, 36H), -2.86 (s, 2H).

MALDI-TOF-MS *m/z* calcd. for $C_{64}H_{62}N_4Si_4$ 998.405 , found 998.260 $[M]^+$.

Synthesis of [5,10,15,20-tetrakis(4-ethynylphenyl)porphinato]iron (III) chloride

[5,10,15,20-tetrakis(4-ethynylphenyl)porphinato]iron (III) chloride (denoted as **1**) was synthesized according to the reported procedure (Scheme S1, STEP 2).[28] The target crystal was obtained from the recrystallization process using CH_2Cl_2 and CH_3OH.

MALDI-TOF-MS *m/z* calcd. for $C_{52}H_{28}FeN_4$ 764.163, found 764.734 $[M]^+$.

Figure 1 shows a schematic of the sample preparation method. Nanoparticles of **1** (denoted as **1**np) were prepared by the reprecipitation method. [35] Specifically, 1 mL of 1 mM solution of **1** dissolved in acetone was added dropwise into 100 mL of pure water under vigorous stirring. The resulting precipitate (**1**np) was then collected by centrifugation. Then, **1**np was carbonized by heating to 600 °C at a rate of 10 °C min^{-1} in a tube furnace under a N_2 atmosphere. Since the structure of **1** meets the necessary requirements for achieving structure-preserving carbonization, [29] OCF can be synthesized simply by carbonizing it in an inert atmosphere. The resulting Fe-

incorporated OCF nanoparticles are denoted as **1**np_600. Reagents and solvents of the best grade available were purchased from commercial suppliers and were used without further purification unless otherwise noted.

2.2. Characterization

^{1}H NMR spectra were recorded on a Bruker Avance III 400 spectrometer and a JEOL ECS 400 spectrometer. ^{1}H chemical shifts were expressed as values relative to tetramethylsilane (TMS). To confirm that the target molecules were certainly obtained, matrix assisted laser desorption/ionization-time of flight-mass spectroscopy (MALDI-TOF-MS) was conducted on a Bruker Autoflex Speed. Scanning electron microscopy (SEM) images were obtained on a Hitachi-S4800. Crystal size and particle size distributions were obtained by dynamic light scattering (DLS-200, Otsuka electronics Co. Ltd.). The thermal decomposition behavior of the precursors were assessed by simultaneous analysis systems including thermogravimetry, and differential scanning calorimetry (TG-DSC). TG-DSC was conducted on a STA 449 Jupiter (Netzsch) from 60 °C to 600 °C at a heating rate of 10 °C min^{-1} under a He flow (150 mL min^{-1}). Powder X-ray diffraction (PXRD) patterns for all the samples were collected using a MiniFlexII (Rigaku Co., Tokyo, Japan) between 2 and 60° (2θ) with a 0.01° step (conditions: Cu-Kα radiation, 45 kV, 15 mA, 1.5418 Å). Transmission electron microscopy (TEM) images of the carbonized samples were obtained using a JEOL JEM-2010 operated at 100 kV. Elemental analysis was conducted using inductively coupled plasma atomic emission spectroscopy (ICP-AES, IRIS Advantage DUO, Thermo Fisher Scientific). Fe K-edge X-ray absorption fine structure (XAFS) spectra were recorded by a transmission mode at the BL01B1 beamline in SPring-8, JASRI, Harima, Japan, using Si (111) monochromator. Fourier transform was applied to the k^3-weighted normalized extended X-ray absorption fine structure (EXAFS) data over the range of $3.0 < k$ (Å^{-1}) < 12 to obtain radial structure functions using Athena and Artemis. [36] Curve fitting analysis for FT-EXAFS spectra was performed using a quick first shell offered by ARTEMIS. [37] The validity of the fitting results was assessed by the R-factor. N_2 adsorption and desorption isotherms were obtained using a BELSORP-MAX system (MicrotracBEL Corp.) at -196 °C. The Brunauer–Emmett–Teller (BET) surface area (S_{BET}) was calculated using the multipoint BET method from the adsorption data in the range of $P/P_0 = 0.01–0.05$. [38] Fe K-edge XAFS spectra of

CP+**1**np electrode before and after electrochemical tests in H_2O_2 under -0.1 V for 15 minutes were recorded by a fluorescence mode at the BL08W XAFS beamline in NanoTerasu, Sendai, Japan, using Si (111) monochromator. Fourier transform was applied to the k^3-weighted normalized EXAFS data over the range of $3.0 < k$ (Å^{-1}) < 9.0 to obtain radial structure functions.

2.3. DFT calculation

To obtain a free energy diagram of the reaction processes of H_2O_2 on pristine graphene and Fe-N_4 embedded graphene, density functional theory (DFT) calculations were performed using the plane-wave self-consistent field (PWscf) code in the Quantum ESPRESSO package. [39-41] All calculations were carried out using the functional proposed by Perdew-Burke-Ernzerhof (PBE) [42] and ultrasoft pseudopotentials [43] with plane-wave and charge-density cutoffs of 25 and 225 Ry, respectively. The DFT-D3 method was applied to describe the van der Waals interactions between the adsorbate and the substrate. [44] In addition, the Hubbard U correction (U = 3.0 eV) was introduced for Fe atoms to account for the on-site Coulomb repulsion among 3d electrons, thereby providing a more accurate description of electronic correlations. [45] Relaxation criteria were 1.0×10^{-4} Ry for the total energy change and 1.0×10^{-3} Ry/Bohr for the maximum allowable forces acting on each atom.

Two slab models were constructed as computational models: (i) a monolayer graphene consisting of 58 carbon atoms with a FeN_4 moiety, and (ii) a monolayer graphene consisting of 64 carbon atoms. [46] A vacuum gap spacing of 20 Å was used to prevent self-interaction. A Monkhorst–Pack k-point samplings of (2 × 2 × 1) were used, and an electron smearing was employed with a width of $k_BT = 0.01$ Ry using the Methfessel–Paxton smearing method to aid k-point convergence. The adsorption energy (E_{ads}) was defined as follows:

$$E_{ads} = E_{Adsorbate/Substrate} - (E_{Substrate} + E_{Adsorbate}) \quad (1)$$

where $E_{Substrate}$ is the total energy of the substrate, $E_{Adsorbate}$ is the total energy of the free adsorbate, and $E_{Adsorbate/Substrate}$ is the energy of the substrate together with the adsorbate. Thus, negative values of E_{ads} correspond to an exothermic adsorption process. In calculating the adsorption energies of H_2O_2 and OH^- on the substrate, the DFT energies of H_2O_2(g) and OH^-(g) were used as $E_{Adsorbate}$, respectively.

The following software was used to create the input files: Winmostar V11, X-Ability Co. Ltd., Tokyo, Japan. All optimized structures, electron density contours, and charge difference plots were visualized using the program VESTA. [47]

2.4. Electrochemical measurement

The basic electrochemical behaviors were analyzed using an electrochemical analyzer, Ivium-n-Stat (Ivium Technologies, Netherlands), with a standard three-electrode system (Figure 2). To prepare a working electrode employing **1**np_600, a paste was prepared by mixing **1**np_600 and JELCON CH-N carbon paste (referred to as CP) at a weight ratio of 22:78. The mixture was coated on a glassy carbon electrode (φ3mm, Bioanalytical Systems, Inc., USA) and dried at 120 °C for 30 min. A counterpart **1**np electrode was prepared in the same way. As a control, an electrode composed solely of CP was also prepared by applying the CP paste onto a glassy carbon electrode and drying in the same manner. An Ag/AgCl electrode containing saturated KCl and a platinum wire were used for the reference and counter electrode, respectively. Cyclic voltammetry (CV) was performed at a scan rate of 10 mV s^{-1} or 100 mV s^{-1}. The detailed experimental conditions are shown with the measurement results. Dulbecco's PBS (D-PBS) and hydrogen peroxide (H_2O_2) were obtained from Fujifilm Wako Pure Chemical Corporation (Japan). The current responses to H_2O_2 were measured by constant potential amperometry at -0.1 V, with H_2O_2 added into D-PBS. During the measurements, the solution was stirred at 200 rpm to ensure uniform mixing of the added H_2O_2, a speed selected to minimize current noise associated with over-stirring.

3. Results and Discussion

3.1. Characterization

The synthesis of the target molecule was confirmed by NMR spectra and MALDI-TOF-MS (p-H-P_4e_TMS and **1**). We conducted the reprecipitation method to obtain **1**np (see 2.1). Figure 3 shows the SEM images of **1** and **1**np (Figure 3a and b), along with their particle size distributions determined by DLS (Figure 3c and d). After the reprecipitation process, particles that were several μm in diameter were reduced to less than 1 μm in size. **1** is observed to consist of a mixture of particles ranging in size from 100 nm to 6 μm (Figure 3a and c), while **1**np is found to have relatively uniform

particles with the size of approximately 260 nm (Figure 3b and d). The thermal behavior of **1** was investigated by TG-DSC measurement (Figure 4). **1** showed a distinct exothermic peak around 200–300 °C, suggesting the thermal polymerization of ethynyl moieties. [27,30,32,48] In the TG curve of **1**, a gradual weight loss was observed, however, **1** showed a high carbonization yield of 94 wt% at 600 °C, similar to the case of using the precursor Ni porphyrin with four ethynyl groups. [30] To investigate the presence of Fe in **1**np_600, we conducted ICP analysis. The elemental composition is summarized in Table 1. The N and Fe contents are well retained after carbonization, and the loading amount of Fe in **1**np_600 was a high loading content of 6.9 wt%. The atomic ratio between N and Fe of **1**np_600 was 3.6:1, which is in good agreement with that of the porphyrin (4:1). This suggests that the structure around the porphyrin remains even after carbonization.

To investigate the local structure around Fe, X-ray absorption fine structure (XAFS) of the Fe-*K* edge was measured. The shapes of the X-ray absorption near edge spectroscopy (XANES) spectra are similar in **1**np and **1**np_600, indicating that the oxidation and the spin states of the Fe in **1**np and **1**np_600 are likely the same (Figure 5a). The oxidation state determined using pre-edge of XANES spectra of **1**np and **1**np_600 were 2.40 and 2.95, respectively (Figure S1). This suggests iron in **1**np_600 is present in trivalent (Fe^{3+}) state. Subsequently, the radial structural functions were calculated using the Fe-*K* edge extended X-ray absorption fine structure (EXAFS) spectra for **1**np, **1**np_600, Fe foil, Fe_2O_3 and Fe_3O_4 (Figure 5b). **1**np exhibits an intense peak at 1.7 Å , corresponding to the N-Fe bound, and this peak is found to be retained after carbonization. In addition, since **1**np_600 does not exhibit the peak around 2.2 Å observed in Fe foil, suggesting that Fe is not aggregated in **1**np_600. Furthermore, the distance between Fe and N and its coordination number were calculated with ARTEMIS (Table S1). The coordination number of **1**np_600 was determined 3.9, which is nearly equivalent to that of **1**np, fixed as 4.

The change of PXRD patterns of **1**np and **1**np_600 are shown in Figure 6. The most intense peak of **1**np at 6 ° is preserved even after heat treatment at 600 °C, indicating that **1**np_600 retains a periodic structure derived from **1**np. Additionally, no peaks corresponding to Fe or iron oxide were observed at higher angles, suggesting that Fe is highly dispersed and does not form particles.

Figure 7 shows N_2 adsorption-desorption isotherms of **1**np and **1**np_600. The adsorption-desorption isotherms showed that **1**np was non-porous, whereas micropores were developed in the carbonized **1**np_600. The micropores are expected to improve the accessibility to the Fe sites. Furthermore, the TEM images of **1**np_600 revealed no aggregation of Fe (Figure S2), which is consistent with the EXAFS and PXRD results, where no Fe-related peaks were detected.

Based on the above results, we successfully synthesized "hemoprotein-like OCF" with porosity, a periodic structure, and a high loading amount of single-atomic iron species.

3.2. Electrochemical characteristics of 1np and 1np_600

To evaluate the electrochemical behavior of **1**np and **1**np_600, we prepared electrodes, each mixed in carbon paste (denoted CP+**1**np electrode and CP+**1**np_600). A carbon paste electrode (CP electrode) was also prepared to evaluate the effect of the carbon paste itself. First, we examined the basic electrochemical behavior and the stability of electrodes in aqueous solution of these electrodes by CV at a scan rate of 100 mV s^{-1}. Figure 8a shows CV curves of CP, CP+**1**np, and CP+**1**np_600 electrodes for the first cycle, measured immediately after immersion in D-PBS (pH 7.4) in air. For the CP electrode, a slight reduction current is observed below -0.1 V, but it remains electrochemically inert overall in the potential range of -0.4 to 0.6 V. In contrast, at CP+**1**np and CP+**1**np_600 electrodes, where CP was mixed with **1**np or **1**np_600, respectively, a reduction current was observed at around -0.1 V or lower, suggesting the reduction of dissolved oxygen. The Fe present in **1**np and **1**np_600 is considered to catalyze oxygen reduction. In particular, a large reduction current was observed in the CP+**1**np electrode, indicating that the precursor **1**np may exhibit a higher oxygen-binding affinity and catalytic activity for the oxygen reduction reaction (ORR) in the first cycle. However, as shown in Figure 8c, the reduction current of the CP+**1**np electrode gradually decreases over the 30 cycles of CV in ambient air. To investigate whether the decrease in reduction current was caused by oxygen depletion, CV curves were recorded in an oxygen-saturated solution using the electrode that had exhibited a decrease in reduction current (Figure S3). As a result, the reduction current increased slightly due to the presence of oxygen, however, the increase was comparable to that observed at the 25th cycle in Figure 8c and did not return to the initial state of the

electrode. The decrease in the reduction current observed in Figure 8c is likely due to iron detachment or the decomposition of **1**np, indicating that the CP+**1**np electrode is not stable in aqueous solution. On the other hand, for the CP+**1**np_600 electrode (Figure 8d), the current remained almost constant with increasing cycle numbers, demonstrating the superior stability of **1**np_600 compared to **1**np. The retention of the reduction current at -0.4 V, normalized to the value of the first cycle (set as 100 %), is presented in Figure 8e. The current retention of **1**np decreased to 17% after 30 cycles, whereas that of CP and CP+**1**np_600 did not decrease but instead increased to 130 %. This suggests that the stability was improved by carbonization. The increase in current retention in CP and CP+**1**np_600 can be attributed to the immediate initiation of measurements after immersing the dry electrodes in the electrolyte, allowing the electrolyte to gradually penetrate the electrodes over time and increase the effective electrode area. Second, after 30 cycles of CV, the effect of dissolved oxygen was evaluated as shown in Figure S4. To minimize the effects of non-Faraday currents, the experiments were conducted at a slower scan rate than that used in Figure 8. As mentioned in Figure 8, for CP+**1**np and CP+**1**np_600 electrodes, it was found that the reduction current below approximately -0.1 V was due to dissolved oxygen. Additionally, the ORR onset potential can be estimated from Figure S4. The ORR onset potential of CP+**1**np_600 electrode is –0.2 V vs. Ag/AgCl, which corresponds to approximately 0.4 V vs. RHE (reversible hydrogen electrode) after correction using the formula: $E_{RHE} = E_{Ag/AgCl} + 0.059 \times pH + 0.1976$. Previously reported iron porphyrin-based materials have exhibited ORR onset potentials in the range of 0.9 to 1.0 V vs. RHE, [49,50] whereas CP+**1**np_600 electrode demonstrated a lower ORR onset potential. This may also be attributed to the electrode preparation method, including factors such as the type and amount of binder used. In this study, we aimed to explore the potential of **1**np_600 as a material for sensing applications. For this purpose, electrodes were prepared by mixing **1**np_600 with a commercially available carbon paste suitable for screen printing. It is considered that this electrode preparation approach may have contributed to the relatively low ORR onset potential observed. Alternatively, a lower ORR onset potential may be beneficial in terms of extending the potential window available for electrochemical measurements.

Hemoproteins, such as catalase and peroxidase, serve as catalysts for redox reactions of hydrogen peroxide. Therefore, to examine the catalytic activity of **1**np and **1**np_600

toward the redox reactions of H_2O_2, we measured CV curves with and without H_2O_2 in D-PBS at a scan rate of 10 mV s^{-1} as shown in Figure 9. In this experiment, the electrodes were preconditioned through 30 cycles of CV scans before use, as shown in Figure 8. For the CP electrode, no significant difference is observed in the CV curves, regardless of the presence of H_2O_2 (Figure 9a). For the CP+**1**np electrode, the reduction current decreases below -0.2 V (Figure. 9b) in the presence of H_2O_2. This is likely due to the low stability of CP+**1**np, which caused a decrease in the reduction current, as shown in Figure 8c, and the continuous degradation of the electrode during the measurement. In contrast, the CP+**1**np_600 electrode exhibits a significant change in its CV curve upon the addition of H_2O_2 (Figure 9c). An oxidation current appears above 0.2 V, and an intense reduction current is observed below 0.2 V, both originating from the redox reactions of H_2O_2 catalyzed by Fe species. This indicates that the catalytic activity for the redox reactions of H_2O_2 can be switched by adjusting the potential, exhibiting behavior similar to that of sensor enzymes, which express biological catalytic activity in response to specific stimuli.

Furthermore, the response stability of the CP+1np_600 electrode to H_2O_2 was evaluated (Figure S5). The electrode that had been immersed in D-PBS for 24 hours after fabrication still responded to H_2O_2, and this responsiveness was maintained on both the second and third days. In addition, since an increase in the reduction current over time was observed even under conditions without H_2O_2, it is possible that water gradually penetrated the electrode during immersion, resulting in an increase of the effective electrode area. To investigate the catalytic mechanism of the Fe site in **1**np_600, DFT calculations were performed. When H_2O_2 was brought close to the Fe site, the adsorption energy was calculated for both horizontal and vertical orientations (Figure S6). It was found that H_2O_2 exhibited stronger adsorption and bond formation in the horizontal orientation. Based on this, free energy diagrams were constructed for the reaction pathways of H_2O_2 on pristine graphene and Fe-N_4 embedded graphene, assuming horizontal H_2O_2 adsorption (Figure 10). The calculations were conducted based on the assumption that the reaction proceeds via adsorption of H_2O_2, followed by its reduction through electron injection, leading to the formation of $2OH^-$. The results indicate that H_2O_2 binds strongly to the Fe site in Fe-N_4 embedded graphene. Furthermore, the formation energies of $2OH^-$ is also larger compared to pristine

graphene, suggesting that the Fe center functions as a catalytic active site for the H_2O_2 reduction reaction.

Leveraging the redox catalysis for H_2O_2, we attempted to detect H_2O_2 using CP+**1**np_600. The current responses were obtained by adding H_2O_2 to D-PBS solution with stirring at 200 rpm under a constant potential at -0.1 V. Figure 11a shows the current response curves of CP, CP+**1**np, and CP+**1**np_600 electrodes. Similar to the findings in Figure 9, CP electrode and CP+**1**np electrode do not respond to H_2O_2. In contrast, for the CP+**1**np_600 electrode, the addition of H_2O_2 results in a reduction current that varied with H_2O_2 concentration, indicating a steady reduction of H_2O_2. The average current value for 10 seconds following 50 seconds after H_2O_2 addition is plotted in Figure 11b. For CP+**1**np_600, the negative current increases linearly with the increase in H_2O_2 concentration up to 2.5 mM. According to the 3σ/S criterion, the calculated LOD for H_2O_2 detection was 455 μM, where σ represents the standard deviation of the blank and S is the slope of the calibration curve. This behavior indicates that **1**np_600 effectively catalyzes the reduction of H_2O_2, which can be used to detect and quantify H_2O_2 in various applications. The observed current response is a direct consequence of the catalytic activity of **1**np_600, confirming its role in the electrochemical reduction process. Finally, to compare the local structure around the Fe sites before and after H_2O_2 exposure, Fe K-edge XAFS measurements were conducted (Figure 12). The XANES spectra and the radial distribution function showed no significant changes even after the electrochemical measurements in H_2O_2, indicating that the oxidation state of Fe species was preserved while maintaining atomic dispersion. These results demonstrate that **1**np_600 is a stable material under reductive conditions and an effective platform for hydrogen peroxide detection, highlighting its potential contribution to the development of advanced electrochemical sensors.

4. Conclusion

We successfully fabricated an electrode using Fe-incorporated OCF (**1**np_600), which largely preserves the porphyrin framework and reactive center. Owing to the carbonized framework, which is fully stabilized at a high temperature, **1**np_600-based electrode worked without degradation or leaching and exhibited high electrochemical stability in an aqueous solution, in contrast to the instability observed in the electrode using the

precursor molecule (**1**np). Furthermore, **1**np_600 exhibited high activity for the reduction of hydrogen peroxide, while also exhibiting activity for the oxidation reaction. This bidirectional catalytic behavior enables the redox reaction to be controlled by potential, effectively mimicking the function of a sensor enzyme. **1**np_600 exhibited a linear reduction current in response to hydrogen peroxide, suggesting its potential application in sensors. DFT calculations further revealed the catalytic behavior of the Fe-N_4 active sites, showing a significantly higher adsorption energy for H_2O_2 compared to pristine graphene, indicating stronger interaction and enhanced activity. XAFS spectroscopy demonstrated that the Fe sites retained their chemical state throughout the catalytic process, highlighting their stability under H_2O_2 exposure. Collectively, these findings underscore the significant potential of Fe-based OCF materials as advanced electrode components. By emulating key functionalities of artificial enzymes and exhibiting reliable electrochemical performance, these materials hold considerable promise for the development of next-generation electrochemical sensing platforms.

Acknowledgements

This work was supported by JST CREST Grant No. JPMJCR24S6; JSPS KAKENHI Grant No. 22KJ0294; JSPS KAKENHI Grant No. 21K14490. The authors appreciate Dr. Fumio Mizutani (Professor Emeritus, University of Hyogo) for his contribution to helpful discussions. The XAFS spectra were recorded at the BL01B1 station in SPring-8, Harima, Japan (Proposal Nos. 2023A1690 and 2023B2097) and at the BL08W XAFS beamline in NanoTerasu, Sendai, Japan. Part of the DFT calculation was performed using supercomputing resources at Cyberscience Center, Tohoku University.

Note

The authors declare no competing financial interest.

References

[1] Antonini E, Brunori M. Hemoglobin and Myoglobin in Their Reactions with Ligands. North-Holland: Amsterdam; 1971.

[2] Sowole MA, Vuong S, Konermann L. Interactions of hemoglobin and myoglobin with their ligands CN(-), CO, and O2 monitored by electrospray

ionization-mass spectrometry. Anal Chem. 2015;87(19):9538-9545. doi: 10.1021/acs.analchem.5b02506

[3] Gell DA. Structure and function of haemoglobins. Blood Cells Mol Dis 2018;70:13-42. doi: 10.1016/j.bcmd.2017.10.006

[4] Maurus R, Overall CM, Bogumil R, et al. A myoglobin variant with a polar substitution in a conserved hydrophobic cluster in the heme binding pocket. Biochim Biophys Acta. 1997;1341(1):1-13. doi: 10.1016/s0167-4838(97)00064-2

[5] Guengerich FP. New trends in cytochrome p450 research at the half-century mark. J Biol Chem. 2013;288(24):17063-17064. doi: 10.1074/jbc.R113.466821

[6] Poulos TL. Heme enzyme structure and function. Chem Rev. 2014;114(7):3919-3962. doi: 10.1021/cr400415k

[7] Cary SPL, Winger JA, Derbyshire ER, Marletta MA. Nitric oxide signaling: no longer simply on or off. Trends Biochem Sci. 2006;31(4):231-239. doi: 10.1016/j.tibs.2006.02.003

[8] Fukuto JM, Carrington SJ, Tantillo DJ, et al. Small molecule signaling agents: the integrated chemistry and biochemistry of nitrogen oxides, oxides of carbon, dioxygen, hydrogen sulfide, and their derived species. Chem Res Toxicol. 2012;25(4):769-93. doi: 10.1021/tx2005234

[9] Baghayeri M, Zare EN, Lakouraj MM. Monitoring of hydrogen peroxide using a glassy carbon electrode modified with hemoglobin and a polypyrrole-based nanocomposite. Microchimica Acta. 2015;182(3-4):771-779. doi: 10.1007/s00604-014-1387-2

[10] Liu Y, Jiang QY, Lu SY, et al. Immobilization of hemoglobin on the gold colloid modified pretreated glassy carbon electrode for preparing a novel hydrogen peroxide biosensor. Appl Biochem Biotechnol. 2009;152(3):418-427. doi: 10.1007/s12010-008-8238-8

[11] Maruyama J, Abe I. Carbonized Hemoglobin Functioning as a Cathode Catalyst for Polymer Electrolyte Fuel Cells. Chem Mater. 2006;18(5):1303-1311. doi: 10.1021/cm0517972

[12] Maruyama J, Hasegawa T, Iwasaki S, et al. Heat Treatment of Carbonized Hemoglobin with Ammonia for Enhancement of Pore Development and Oxygen Reduction Activity. ACS Sustainable Chemistry & Engineering. 2013;2(3):493-499. doi: 10.1021/sc400402y

[13] Ding Y, Jia W, Zhang H, et al. Carbonized Hemoglobin Nanofibers for Enhanced H_2O_2 Detection. Electroanalysis. 2010;22(16):1911-1917. doi: 10.1002/elan.200900595

[14] Shimizu T, Huang D, Yan F, et al. Gaseous O2, NO, and CO in signal transduction: structure and function relationships of heme-based gas sensors and heme-redox sensors. Chem Rev. 2015;115(13):6491-6533. doi: 10.1021/acs.chemrev.5b00018

[15] Wang JH. Hemoglobin studies. II. A synthetic material with hemoglobin-like property. J Am Chem Soc. 1958;80(12):3168-3169. doi: 10.1021/ja01545a072

[16] Hamachi I, Tsukiji S, Shinkai S, Oishi S. Direct Observation of the Ferric-Porphyrin Cation Radical as an Intermediate in the Phototriggered Oxidation of Ferric- to Ferryl-Heme Tethered to $Ru(bpy)_3$ in Reconstituted Myoglobin. J Am Chem Soc. 1999;121(23):5500-5506. doi: 10.1021/ja984199f

[17] Kurosawa M, Itoh T, Kodera Y, et al. Formation of a bioconjugate composed of hemin, smectite, and quaternary ammonium chloride that is soluble and active in

hydrophobic media. Bioconjug Chem. 2002;13(2):167-71. doi: 10.1021/bc000133+

[18] Itoh T, Yano K, Kajino T, et al. Phytol-modified heme in mesoporous silica: conjugates as models of hemoproteins. Biotechnol Bioeng. 2006;93(3):476-484. doi: 10.1002/bit.20734

[19] Yu W, Shen Z, Yoshii T, et al. Hierarchically Porous and Minimally Stacked Graphene Cathodes for High-Performance Lithium–Oxygen Batteries. Advanced Energy Materials. 2023;14(2):2303055. doi: 10.1002/aenm.202303055

[20] Tanaka D, Takemori N, Iba Y, et al. Cobalt-catalyzed carbonization from polyacrylonitrile for preparing nitrogen-containing ordered mesoporous carbon CMK-1 electrode with high electric double-layer capacitance. Microporous and Mesoporous Materials. 2024;379:113294. doi: 10.1016/j.micromeso.2024.113294

[21] Itoi H, Saeki G, Usami T, et al. Activation-Free Synthesis of Chitin-Derived Porous Carbon: Application for Electrical Energy Storage. ACS Sustainable Resource Management. 2024;1(4):743-756. doi: 10.1021/acssusresmgt.3c00127

[22] Hatakeyama Y, Naito H, Oda R, Shiraishi S. Investigation of the effect of load weight on the discharge capacity of lithium–O2 batteries using carbon-paper–based electrodes. Journal of Energy Storage. 2024;91:111974. doi: 10.1016/j.est.2024.111974

[23] Hu M, Reboul J, Furukawa S, et al. Direct synthesis of nanoporous carbon nitride fibers using Al-based porous coordination polymers (Al-PCPs). Chem Commun. 2011;47:8124-8126. doi: 10.1039/C1CC12378E

[24] Jiang HL, Liu B, Lan YQ, et al. From metal-organic framework to nanoporous carbon: toward a very high surface area and hydrogen uptake. J Am Chem Soc. 2011;133(31):11854-11857. doi: 10.1021/ja203184k

[25] Kayahara E, Iwamoto T, Takaya H, et al. Synthesis and physical properties of a ball-like three-dimensional pi-conjugated molecule. Nat Commun. 2013;4:2694. doi: 10.1038/ncomms3694

[26] Nishihara H, Hirota T, Matsuura K, et al. Synthesis of ordered carbonaceous frameworks from organic crystals. Nat Commun. 2017;8(1):109. doi: 10.1038/s41467-017-00152-z

[27] Nishihara H, Matsuura K, Ohwada M, et al. Synthesis of Ordered Carbonaceous Framework with Microporosity from Porphyrin with Ethynyl Groups. Chemistry Letters. 2020;49(6):619-623. doi: 10.1246/cl.200141

[28] Yamamoto M, Takahashi K, Ohwada M, et al. Iron porphyrin-derived ordered carbonaceous frameworks. Catalysis Today. 2021;364:164-171. doi: 10.1016/j.cattod.2020.07.003

[29] Yoshii T, Chida K, Nishihara H, Tani F. Ordered carbonaceous frameworks: a new class of carbon materials with molecular-level design. Chem Commun (Camb). 2022;58(22):3578-3590. doi: 10.1039/d1cc07228e

[30] Chida K, Yoshii T, Ohwada M, et al. Synthesis and electrocatalysis of ordered carbonaceous frameworks from Ni porphyrin with four ethynyl groups. Catalysis Today. 2023;411-412:113830. doi: 10.1016/j.cattod.2022.06.045

[31] Chida K, Yoshii T, Hiyoshi N, et al. Bimetallic ordered carbonaceous frameworks from Co- and Cu-porphyrin bimolecular crystals. Carbon. 2023;201:338-346. doi: 10.1016/j.carbon.2022.09.017

[32] Chida K, Yoshii T, Takahashi K, et al. Force-responsive ordered carbonaceous frameworks synthesized from Ni-porphyrin. Chem Commun (Camb). 2021;57(49):6007-6010. doi: 10.1039/d1cc01618k

[33] Sano Y, Toyoda R, Chida K, et al. Ordered Carbonaceous Framework Synthesized from Hexaazatrinaphthylene with Enediyne Groups via Solid-State Bergman Cyclization Reaction. ACS Appl Mater Interfaces. 2024 ;16(32):42615-42622. doi: 10.1021/acsami.4c06959

[34] Yao D, Zhang X, Mongin O, et al. Synthesis and Characterization of New Conjugated Fluorenyl-Porphyrin Dendrimers for Optics. Chemistry. 2016;22(16):5583-97. doi: 10.1002/chem.201504617

[35] Kasai H, Nalwa HS, Oikawa H, et al. A novel preparation method of organic microcrystals. Japanese Journal of Applied Physics. 1992;31(8):L1132-L1134. Doi: 10.1143/JJAP.31.L1132

[36] Ravel B, Newville M. ATHENA, ARTEMIS, HEPHAESTUS: data analysis for X-ray absorption spectroscopy using IFEFFIT. J Synchrotron Radiat. 2005;12(4):537-541. doi: 10.1107/S0909049505012719

[37] Ma K, Zhao L, Jiang Z, et al. Adsorption characteristics of Cr (III) onto starch‐graft‐poly(acrylic acid)/organo‐modifed zeolite 4A composite: A novel path to the adsorption mechanisms. Polymer Composites. 2018;39(4):1223-1233. doi: 10.1002/pc.24056

[38] Kaneko K, Ishii C. Superhigh surface area determination of microporous solids. Colloids and Surfaces. 1992;67:203-212. doi: 10.1016/0166-6622(92)80299-H

[40] Giannozzi P, Baseggio O, Bonfà P, et al. Quantum ESPRESSO toward the exascale. J. Chem. Phys. 2020;152(15):154105. doi: 10.1063/5.0005082

[41] Giannozzi P, Andreussi O, Brumme T, et al. Advanced capabilities for materials modelling with Quantum ESPRESSO. J. Phys. -Condens. Matter. 2017;29(46):465901.doi: 10.1088/1361-648X/aa8f79

[42] Perdew JP, Burke K, Ernzerhof M. Generalized Gradient Approximation Made Simple. Phys. Rev. Lett. 1996;77(18):3865-3868. doi: 10.1103/PhysRevLett.77.3865

[43] Vanderbilt D. Soft self-consistent pseudopotentials in a generalized eigenvalue formalism. Phys. Rev. B. 1990;41(11):7892-7895. dol: 10.1103/physrevb.41.7892

[44] Grimme S, Antony J, Ehrlich S, Krieg H. A consistent and accurate ab initio parametrization of density functional dispersion correction (DFT-D) for the 94 elements H-Pu. J. Chem. Phys. 2010;132(15):154104. doi: 10.1063/1.3382344

[45] Orellana W, Miwa RH. Fe and Co adatoms on bilayer borophene as single-atom catalysts for the oxygen-reduction reaction: A theoretical study. Phys. Rev. Appl. 2024;21:034008. doi: 10.1103/PhysRevApplied.21.034008

[46] Yu W, Yoshii T, Aziz A, et al. Edge-Site-Free and Topological-Defect-Rich Carbon Cathode for High-Performance Lithium-Oxygen Batteries. Adv Sci. 2023:e2300268. doi: 10.1002/advs.202300268

[47] Momma K, Izumi F. VESTA 3 for three-dimensional visualization of crystal, volumetric and morphology data. J. Appl. Crystallogr. 2011;44(6):1272-1276. doi: 10.1107/s0021889811038970

[48] Chida K, Yoshii T, Kawaguchi R, et al. Rational bottom-up synthesis of sulphur-rich porous carbons for single-atomic platinum catalyst supports. Green Chemistry. 2024;26(15):8758-8767. doi: 10.1039/d4gc02055c

[49] Jiao L, Wan G, Zhang R, et al. From Metal-Organic Frameworks to Single-Atom Fe Implanted N-doped Porous Carbons: Efficient Oxygen Reduction in

Both Alkaline and Acidic Media. Angew Chem Int Ed Engl. 2018;57(28):8525-8529. doi: 10.1002/anie.201803262

[50] Chen Y, Ji S, Wang Y, et al. Isolated Single Iron Atoms Anchored on N-Doped Porous Carbon as an Efficient Electrocatalyst for the Oxygen Reduction Reaction. Angew Chem Int Ed Engl. 2017 Jun 6;56(24):6937-6941. doi: 10.1002/anie.201702473

Figures and Tables

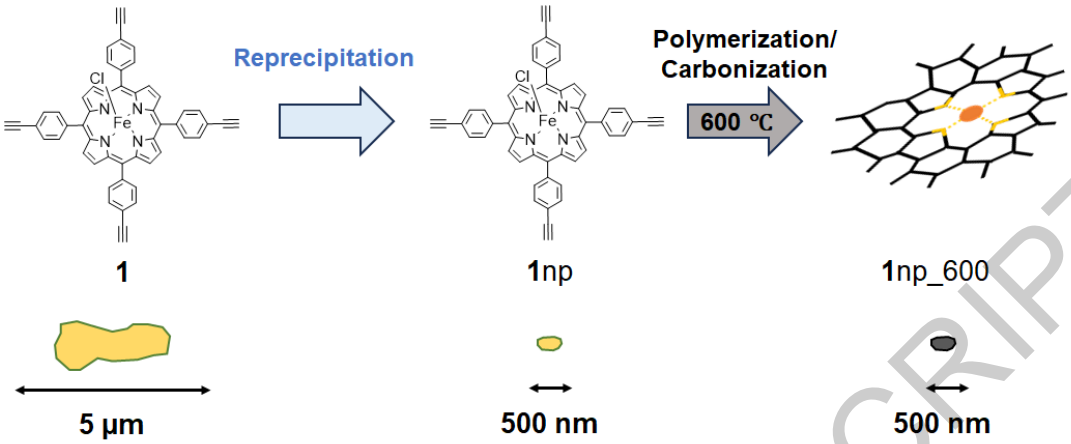

Figure 1. Schematic of the sample preparation method.

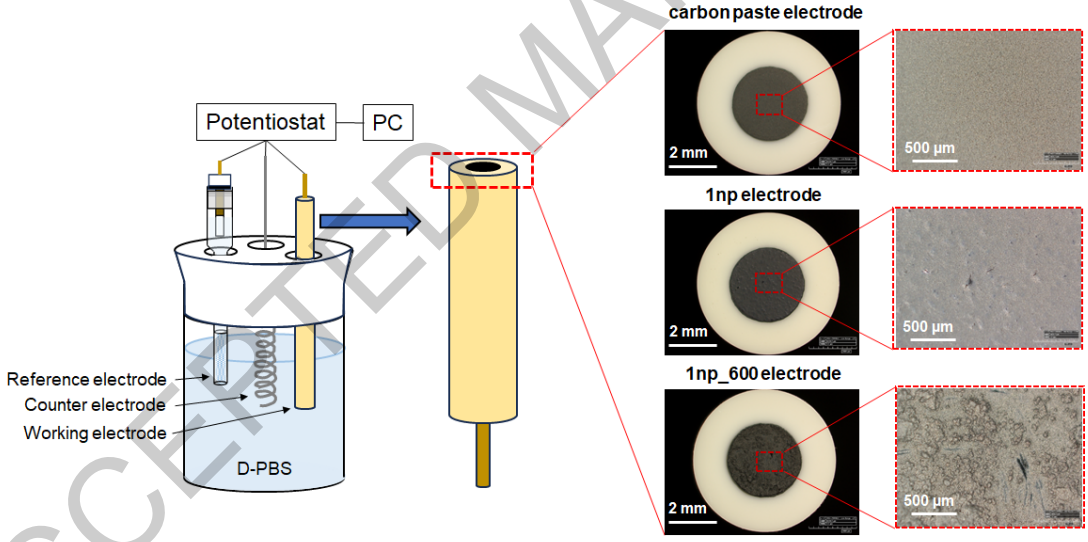

Figure 2. Schematic diagram of the electrochemical cell setup.

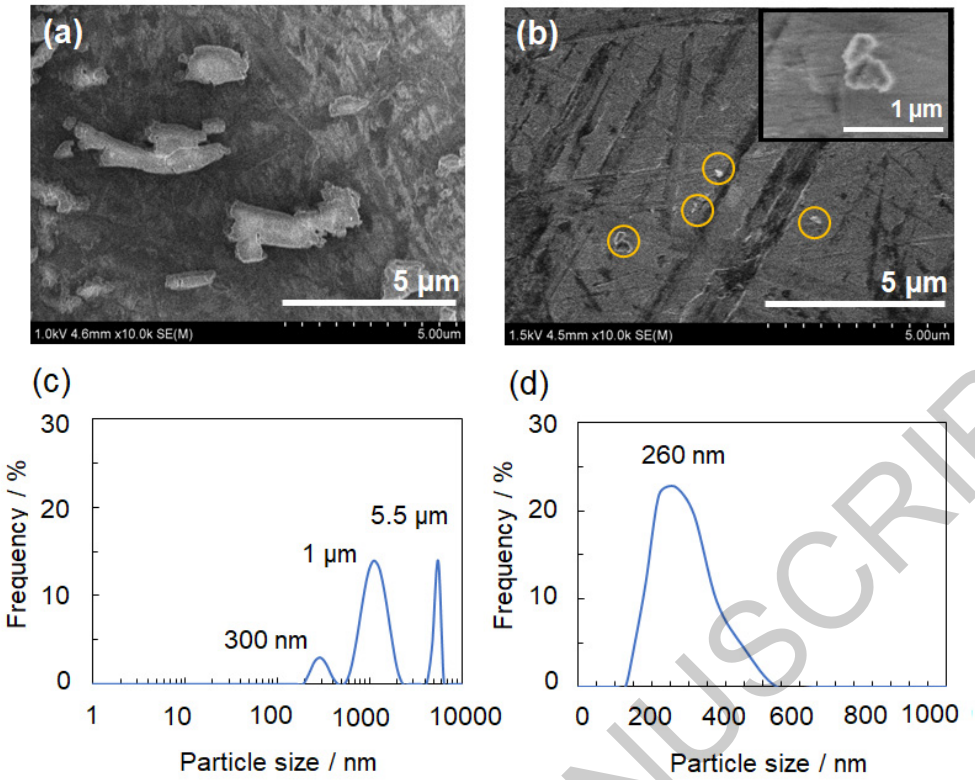

Figure 3. SEM images of (a) **1** and (b) **1**np. Particle size distribution of (c) **1** and (d) **1**np by DLS.

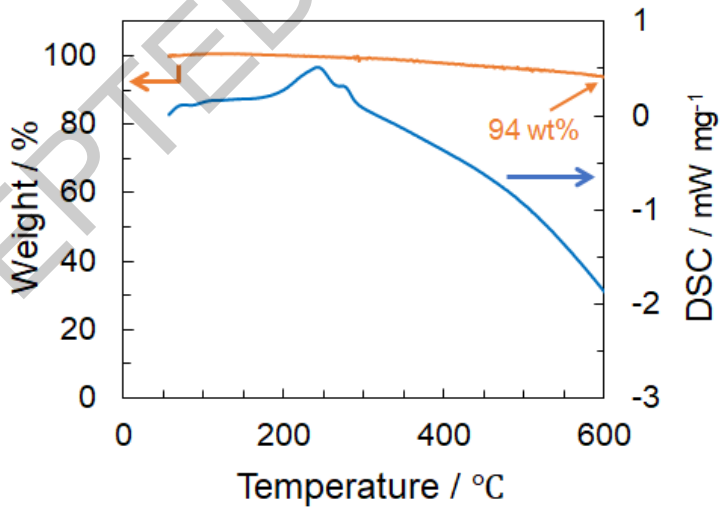

Figure 4. TG-DSC curves of **1**. TG curve is orange line and DSC curve is bule line.

Table 1. Elemental compositions of **1**np and **1**np_600.

	Elemental composition (wt%)				
Sample	C	H	N	Fe	Cl
1np [a]	77.6	4.13	6.98	6.96	4.42
1np	75.0	3.9	6.6	6.0	3.1
1np_600	66.9	3.4	6.2	6.9	0.2

[a] calculated from chemical formula.

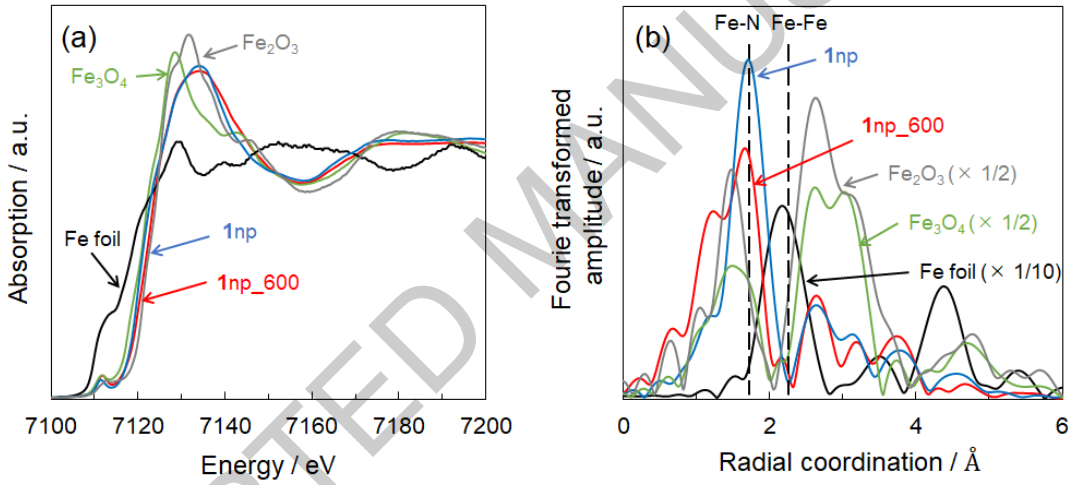

Figure 5. X-ray absorption fine structure results of **1**np (blue line) and **1**np_600 (red line). (a) XANES spectra. (b)Radial structural functions calculated from EXAFS patterns. The data of Fe foil (black line), Fe_2O_3 (gray line) and Fe_3O_4 (green line) are shown for comparison.

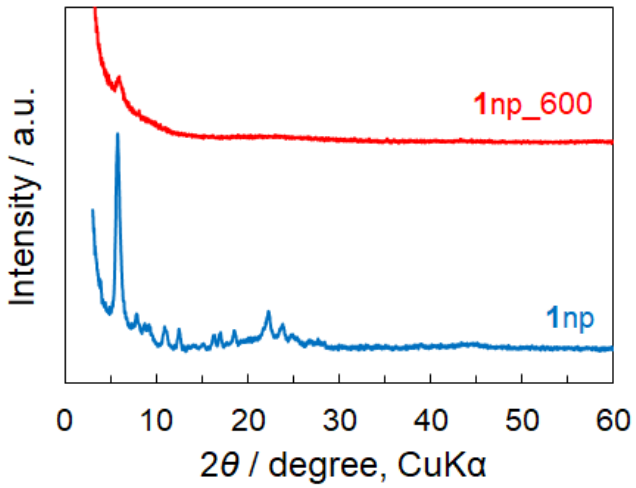

Figure 6. The change of PXRD patterns of **1**np and upon heat treatment.

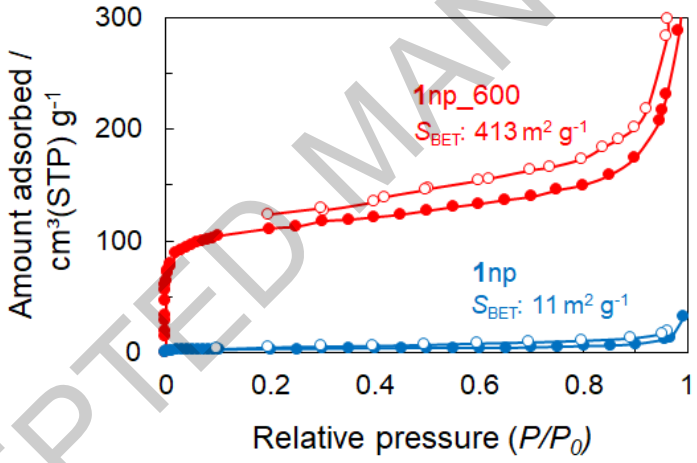

Figure 7. N_2 adsorption-desorption isotherms of **1**np (blue) and **1**np_600 (red). Closed circles indicate adsorption and opened circles indicate desorption.

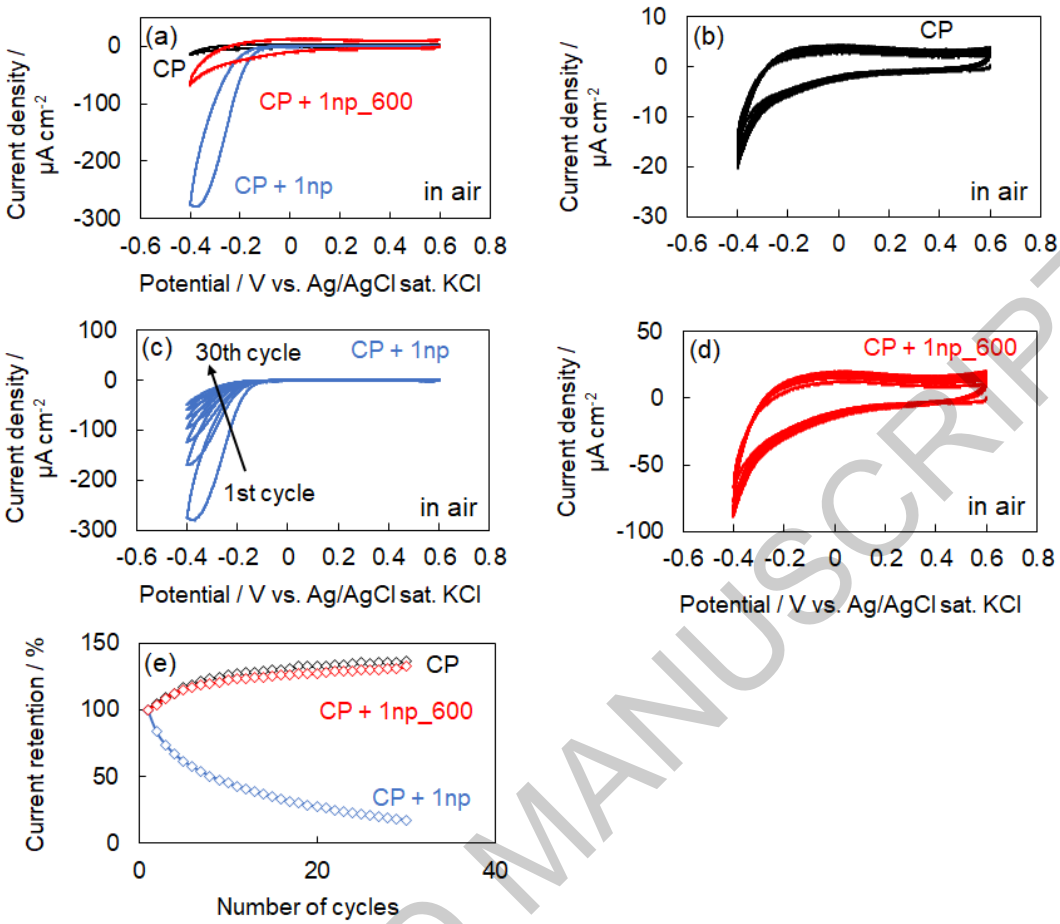

Figure 8. (a) Cyclic voltammograms of CP electrode, CP+**1**np electrode, and CP+**1**np_600 electrode immediately after immersion in D-PBS. The First cycles are shown. Cyclic voltammograms of (b) CP electrode, (c) CP+**1**np electrode, and (d) CP+**1**np_600 electrode. 30 cycles were repeated. 1st, 5th, 10th, 15th, 20th, 25th, 30th cycles are shown. (e) Cyclic stability of each electrode plotted reduction current at -0.4 V from CV curves for 30 cycles. All cyclic voltammograms were measured at a scan rate of 100 mV s^{-1} with a potential range of -0.4 V to 0.6 V in air.

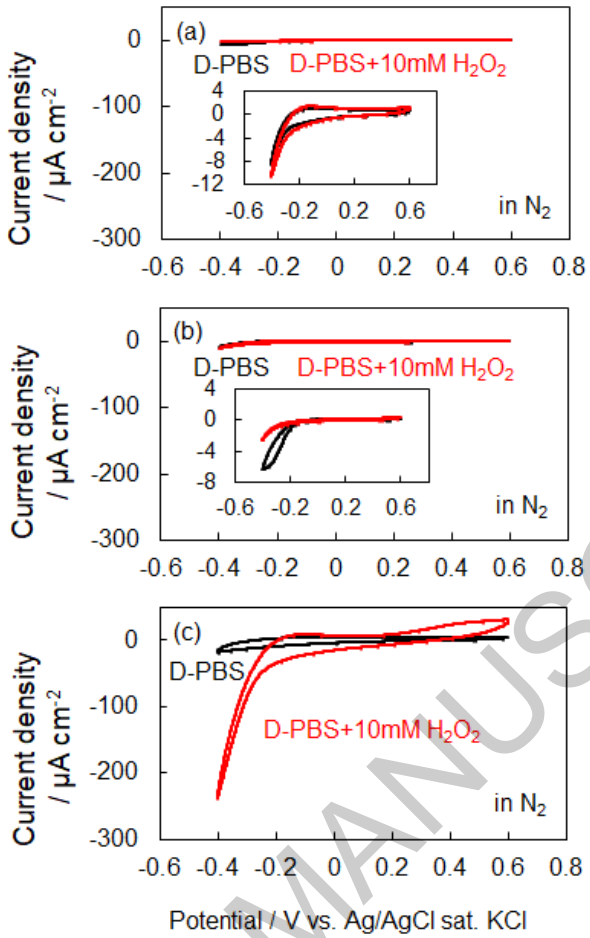

Figure 9. Cyclic voltammograms of (a) CP electrode, (b) CP+**1**np electrode, and (c) CP+**1**np_600 electrode, measured in the absence and presence of H_2O_2 in D-PBS at a scan rate of 10 mV s^{-1}. The solutions were purged by N_2 gas.

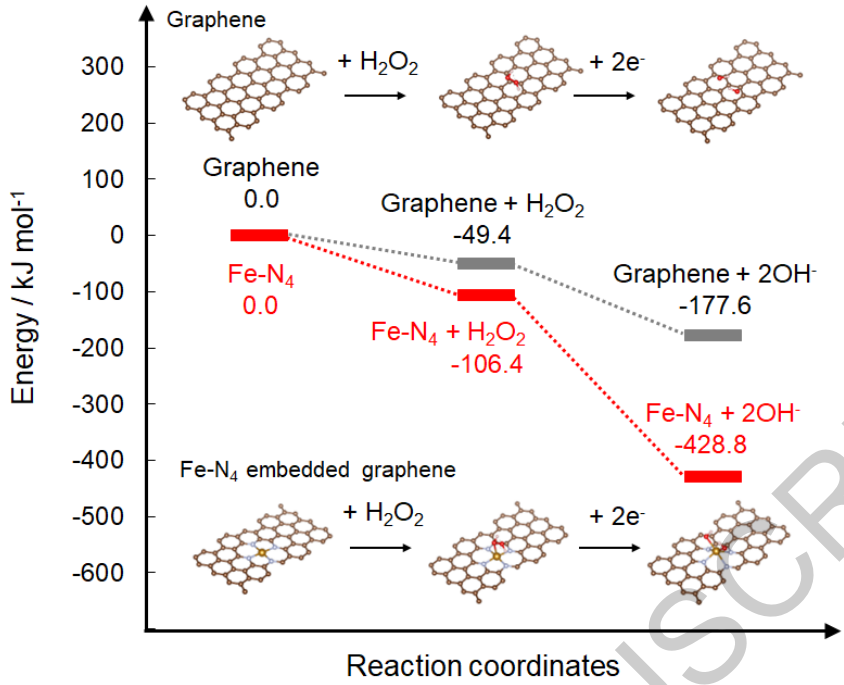

Figure 10. Calculated energy diagram for the H_2O_2 reaction processes on pristine graphene (gray) and Fe-N_4 embedded graphene (red). Schematic representations of the H_2O_2 reaction pathways on pristine graphene and Fe-N_4 embedded graphene. Carbon, oxygen, hydrogen, nitrogen, and iron atoms are shown in brown, red, white, blue, and yellow, respectively.

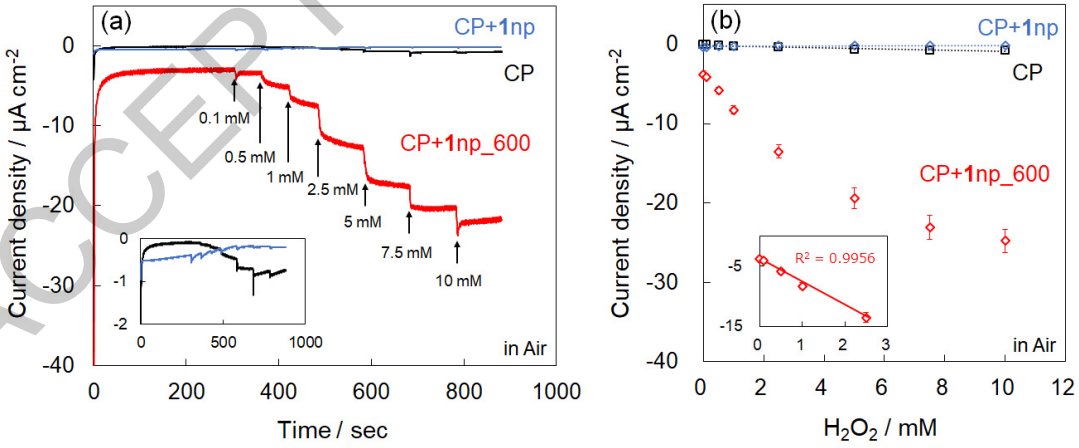

Figure 11. (a) Amperometric response to of CP electrode (black), CP+**1**np electrode (blue), and CP+**1**np_600 electrode successive addition of different concentration of H_2O_2 in D-PBS at the working potential of −0.1 V vs. Ag/AgCl sat. KCl in air. (b) Calibration curves of H_2O_2 concentration.

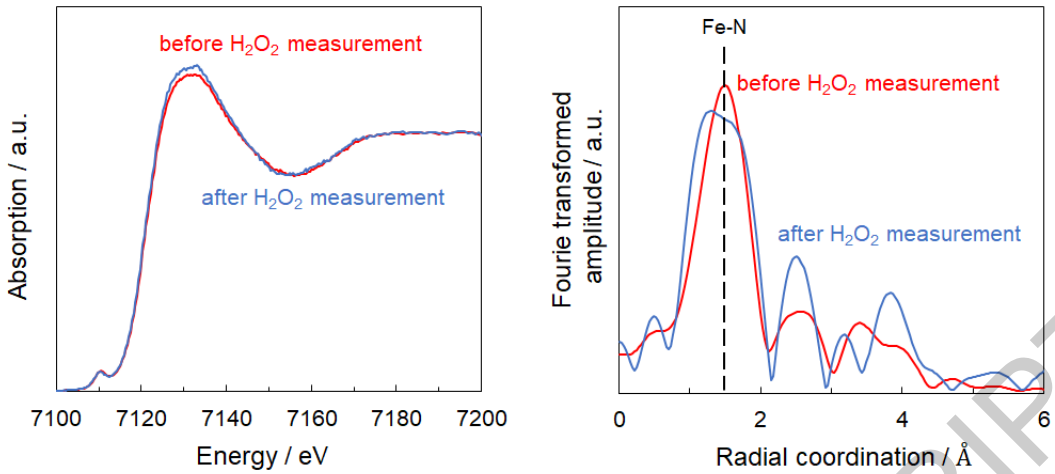

Figure 12. (a) X-ray absorption fine structure results of before (red line) and after (bule line) H_2O_2 measurements. (a) XANES spectra. (b) Radial structural functions calculated from EXAFS patterns.

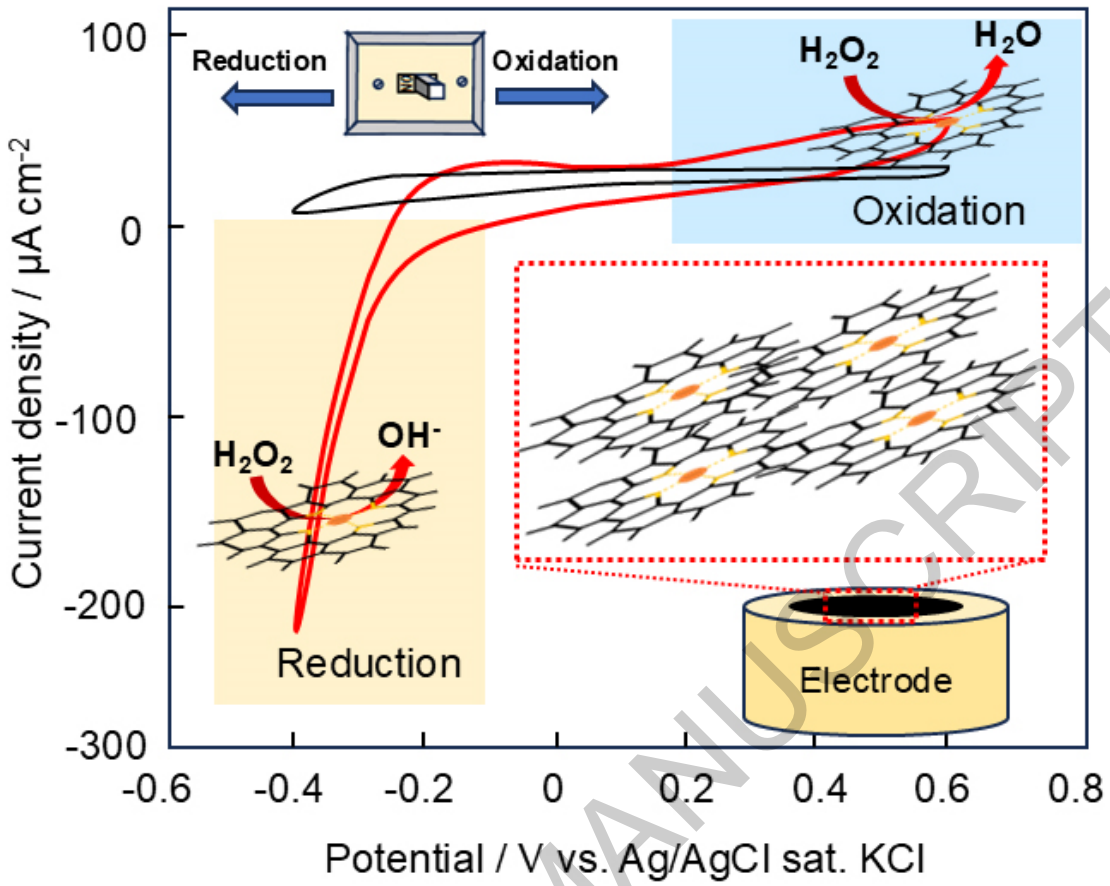

Graphical Abstract